Nuclear fusion reaction rates for strongly coupled ionic mixtures

A. I. Chugunov
Ioffe Physical-Technical Institute, Politekhnicheskaya 26, RU-194021 St. Petersburg, Russia

H. E. DeWitt
Lawrence Livermore National Laboratory, Livermore, California 94550, USA
(Received 17 April 2009; published 31 July 2009)

We analyze the effect of plasma screening on nuclear reaction rates in dense matter composed of atomic nuclei of one or two types. We perform semiclassical calculations of the Coulomb barrier penetrability taking into account a radial mean-field potential of plasma ions. The mean-field potential is extracted from the results of extensive Monte Carlo calculations of radial pair distribution functions of ions in binary ionic mixtures. We calculate the reaction rates in a wide range of plasma parameters and approximate these rates by an analytical expression that is expected to be applicable to multicomponent ion mixtures. Also, we analyze Gamow-peak energies of reacting ions in various nuclear burning regimes. For illustration, we study nuclear burning in ^{12}C-^{16}O mixtures.

DOI: 10.1103/PhysRevC.80.014611 PACS number(s): 26.30.−k

I. INTRODUCTION

Nuclear fusion in dense stellar matter is most important in the evolution of all stars. The main source of energy for main-sequence stars is provided by hydrogen and helium burning. The subsequent burning of carbon and heavier elements [1] drives an ordinary star along the giant/red-giant branch to its final moments as a normal star. Nuclear burning is also important for compact stars. It is the explosive burning of carbon and other elements in the cores of massive white dwarfs; it triggers type Ia supernova explosions (see, e.g., Ref. [2] and references therein). Explosive burning in the envelopes of neutron stars can produce type I x-ray bursts [3] and superbursts (which have been observed from some x-ray bursters, e.g., in Refs. [4,5]). Accreted matter that penetrates into deep layers of the neutron star crust undergoes pycnonuclear reactions. Nuclear reactions can also power thermal radiation observed from neutron stars in soft x-ray transients in quiescent states (see, e.g., Refs. [5–13]). Thus, nuclear reactions are important in stars at all evolutionary stages.

It is well known that nuclear reaction rates in dense matter are determined by astrophysical S factors, which characterize the nuclear interaction of fusing atomic nuclei, and by the Coulomb barrier penetration preceding the nuclear interaction. We will mostly focus on the Coulomb barrier penetration problem. Fusion reactions in ordinary stars proceed in the so-called classical thermonuclear regime in which ions (atomic nuclei) constitute a nearly ideal Boltzmann gas. In this case, the Coulomb barrier between reacting nuclei is almost unaffected by plasma screening effects produced by neighboring plasma particles. The Coulomb barrier penetrability is then well defined.

However, in the dense matter of white dwarf cores and neutron star envelopes the ions form a strongly nonideal Coulomb plasma, where the plasma screening effects can be very strong. The plasma screening greatly influences the barrier penetrability and the reaction rates. Depending on the density and temperature of the matter, nuclear burning can proceed in four other regimes [14]. They are the thermonuclear regime with strong plasma screening, the intermediate thermo-pycnonuclear regime, the thermally enhanced pycnonuclear regime, and the pycnonuclear zero-temperature regime. The reaction regimes will be briefly discussed in Sec. II A. In these four regimes, the calculation of the Coulomb barrier penetration is complicated. There have been many attempts to solve this problem using several techniques, but the exact solution is still a subject of debates (see Refs. [15–17] and reference therein).

In our previous paper [17], we studied nuclear reactions in a one-component plasma (OCP) of ions. Now we extend our consideration to binary ionic mixtures (BIMs). In Sec. II, we discuss physical conditions and reaction regimes. In Sec. III, we describe the results of our most extensive and accurate Monte Carlo calculations, analyze them, and use them to parametrize the mean-field potential. In Sec. IV, this potential is employed to calculate the enhancement factors of nuclear reaction rates. We study the Gamow-peak energies and the effects of plasma screening on astrophysical S factors in Sec. V. Section VI is devoted to the analysis of the results. We conclude in Sec. VII. In the Appendix, we suggest a simple generalization of our results to the cases of weak and moderate Coulomb coupling of ions.

II. PHYSICAL CONDITIONS AND REACTION REGIMES

A. Nuclear reaction regimes

We consider nuclear reactions in the dense matter of white dwarf cores and outer envelopes of neutron stars. This matter contains atomic nuclei (ions, fully ionized by electron pressure) and strongly degenerate electrons, which form an almost uniform background of negative charge. For simplicity, we will not consider the inner crust of neutron stars (with density higher than the neutron drip density of

$\sim 4 \times 10^{11}\,\mathrm{g\,cm^{-3}}$ [18]), which contains also free degenerate neutrons.

We will generally study a multicomponent mixture of ions $j = 1, 2, \ldots$ with atomic mass numbers A_j and charge numbers Z_j. The total ion number density can be calculated as $n_\mathrm{i} = \sum_j n_j$, where n_j is a number density of ions j. It is useful to introduce the fractional number $x_j = n_j/n_\mathrm{i}$ of ions j. Let us also define the average charge number $\langle Z\rangle = \sum_j x_j Z_j$ and mass number $\langle A\rangle = \sum_j x_j A_j$ of ions. The charge neutrality implies that the electron number density is $n_e = \langle Z\rangle n_\mathrm{i}$. The electron contribution to the mass density ρ can be neglected, so that $\rho \approx \langle A\rangle m_u n$, where $m_u \approx 1.66054 \times 10^{-24}$ g is the atomic mass unit.

The importance of the Coulomb interaction for ions j can be described by the coupling parameter Γ_j

$$\Gamma_j = \Gamma_{jj} = \frac{Z_j^2 e^2}{a_j k_B T}, \quad a_j = Z_j^{1/3} a_e, \quad a_e = \left(\frac{3}{4\pi n_e}\right)^{1/3}, \tag{1}$$

where a_j and a_e are the ion-sphere and electron-sphere radii, k_B is the Boltzmann constant, and T is the temperature. Note, that the electron charge within an ion sphere exactly compensates the ion charge $Z_j e$; Γ_j gives the ratio of characteristic electrostatic energy $Z_j^2 e^2/a_j$ to the thermal energy $k_B T$.

If $\Gamma_j \ll 1$, the ions constitute an almost ideal Boltzmann gas, while for $\Gamma_j \gtrsim 1$ they are strongly coupled by Coulomb forces and constitute either a Coulomb liquid or solid. The transformation from the gas to the liquid at $\Gamma_j \sim 1$ is smooth, without any phase transition. According to highly accurate Monte Carlo calculations, a classical OCP of ions solidifies at $\Gamma \approx 175$ (see, e.g., Ref. [19]).

We will discuss fusion reactions

$$(A_i, Z_i) + (A_j, Z_j) \to \left(A_{ij}^\mathrm{comp}, Z_{ij}^\mathrm{comp}\right), \tag{2}$$

where $A_{ij}^\mathrm{comp} = A_i + A_j$ and $Z_{ij}^\mathrm{comp} = Z_i + Z_j$ refer to a compound nucleus. The reaction rate is determined by an astrophysical S factor and by the Coulomb barrier penetration problem. For a nonresonant reaction, the S factor is a slowly varying function of energy (see, e.g., Ref. [16]). It is determined by the short-range nuclear interaction of fusing nuclei. The Coulomb barrier penetration problem can be reduced to the calculation of the contact probability $g_{ij}(0)$, which is the value of the quantummechanical pair correlation function of reacting nuclei i and j at small distances $r \to 0$. Finally, the reaction rate can be written as (see Sec. V and Ref. [20])

$$R_{ij} = \frac{2\,a_{ij}^B}{(1+\delta_{ij})\pi\hbar}\, n_i\, n_j S_{ij}\left(E_{ij}^{\mathrm{pk}'}\right) g_{ij}(0), \tag{3}$$

where

$$S_{ij}(E) = \sigma_{ij}(E) E \exp(2\pi\eta_{ij}) \tag{4}$$

is the astrophysical factor. It should be taken at an appropriate energy $E = E_{ij}^{\mathrm{pk}'}$, which is the "Gamow-peak energy," corrected for the plasma screening (see Sec. V and Fig. 6); δ_{ij} is Kronecker delta, which excludes double counting of the same collisions in reactions of identical nuclei ($i = j$).

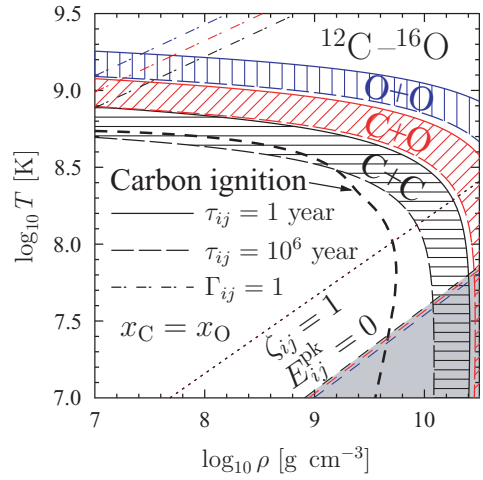

FIG. 1. (Color online) Temperature-density diagram for ^{12}C + ^{16}O mixture with equal number densities of ^{12}C and ^{16}O. The dash-dot lines correspond (from top to bottom) to $\Gamma_{\mathrm{OO}}, \Gamma_{\mathrm{CO}}, \Gamma_{\mathrm{CC}} = 1$. For temperatures below these lines, the effects of plasma screening on corresponding reaction rates become strong. The dotted line is $\zeta_{ij} = 1$. This line is the same for all i and j because of the same $A/Z = 2$ ratio. The reacting nuclei become bound along the dashed straight lines (the Gamow-peak energy passes through zero, see Sec. V). For lower temperatures (gray region) the mean-field model (used in this paper) becomes inadequate. The shaded regions are bound by solid and long-dashed lines of constant burning times (1 yr and 10^6 yr). The thick dash line is the carbon ignition curve (Sec. VI).

For these reactions, $a_{ij}^B = \hbar^2/\left(2\mu_{ij}\, Z_i\, Z_j\, e^2\right)$ reduces to the ion Bohr radius. Furthermore, $\mu_{ij} = m_u\, A_i A_j / A_{ij}^\mathrm{comp}$ is the reduced mass of the nuclei, and $\sigma_{ij}(E)$ is the fusion cross section. Finally, $\eta_{ij} = Z_i Z_j e^2 \sqrt{\mu_{ij}/(2E\hbar^2)}$ determines the penetrability of the Coulomb barrier.

Figure 1 is the temperature-density diagram for a ^{12}C + ^{16}O mixture with equal number densities of both species. Also, we present the lines of constant dimensionless parameters (see Sec. II B) $\Gamma_{ij} = 1$ (dash-dot lines) and $\zeta_{ij} = 1$ (the dotted line). The dash-dot lines (from top to bottom) correspond to $\Gamma_{\mathrm{OO}} = 1$, $\Gamma_{\mathrm{CO}} = 1$, and $\Gamma_{\mathrm{CC}} = 1$. The $\zeta_{ij} = 1$ line is the same for all combinations of ions because of equal $A/Z = 2$ ratios for ^{12}C and ^{16}O ions. The shaded regions are bounded by the solid and long-dashed lines of constant burning times of 1 and 10^6 yr, respectively. The region for the O+O reaction is highest, for C+O intermediate, and for C+C lowest (as regulated by the height of the Coulomb barrier). The lines of constant burning time are similar. At $\rho \lesssim 10^9\,\mathrm{g\,cm^{-3}}$ they mainly depend on temperature because of exponentially strong temperature dependence of the reaction rates. These parts of the lines correspond to thermonuclear burning (with weak or strong plasma screening). With growing density, the curves bend and become nearly vertical (which corresponds to the pycnonuclear burning due to zero-point vibrations of atomic nuclei; see Refs. [14,16,21,22]). The pycnonuclear reaction rate is a rapidly varying function of density, which is either slightly dependent on or almost independent of temperature.

The carbon ignition curve (discussed in Sec. VI) is shown by the thick dashed line.

B. Dimensionless parameters

Let us consider a binary mixture of ions with mass numbers A_1 and A_2, charge numbers Z_1 and Z_2, and fractional numbers $x_1 = n_1/n_i$ and $x_2 = 1 - x_1$. Following Itoh *et al.* [23], in addition to the ion radii $a_i = a_{ii}$ we introduce an effective radius

$$a_{12} = \frac{a_1 + a_2}{2} = \frac{Z_1^{1/3} + Z_2^{1/3}}{2}\, a_e. \tag{5}$$

It is also convenient to define the parameter

$$\Gamma_e = e^2/(a_e\, k_B\, T). \tag{6}$$

The coupling parameters for ions can be written as

$$\Gamma_i = \Gamma_{ii} = \Gamma_e\, Z_i^{5/3}. \tag{7}$$

In addition, we introduce an effective Coulomb coupling parameter

$$\Gamma_{12} = Z_1 Z_2 e^2/(a_{12} k_B\, T), \tag{8}$$

to be used later for studying a reaction of the type $(A_1, Z_1) + (A_2, Z_2)$.

Furthermore, we introduce the corresponding ion radius and the Coulomb coupling parameter for a compound nucleus $(A_i + A_j, Z_i + Z_j) = (A_{ij}^{\rm comp}, Z_{ij}^{\rm comp})$,

$$a_{ij}^{\rm comp} = a_e \left(Z_{ij}^{\rm comp}\right)^{1/3}, \quad \Gamma_{ij}^{\rm comp} = \Gamma_e \left(Z_{ij}^{\rm comp}\right)^{5/3}. \tag{9}$$

The Coulomb barrier penetrability in the classical thermonuclear regime (neglecting plasma screening) is characterized by the parameter

$$\tau_{ij} = \left(\frac{27\pi^2 \mu_{ij} Z_i^2 Z_j^2 e^4}{2 k_B T \hbar^2}\right)^{1/3}. \tag{10}$$

The Gamow-peak energy in this regime is

$$E_{ij}^{\rm pk} = k_B T\, \tau_{ij}/3. \tag{11}$$

The effects of plasma screening on the Gamow-peak energy and tunneling range are discussed in Sec. V.

Also, we introduce the dimensionless parameter

$$\zeta_{ij} = 3\, \Gamma_{ij}/\tau_{ij}. \tag{12}$$

In a OCP, ζ_{ii} reduces to the parameter ζ defined in Ref. [17] and has a simple meaning: it is the ratio of the tunneling length of nuclei with the Gamow-peak energy (calculated neglecting the plasma screening effects) to the ion sphere radius a_{ij}.

III. MEAN-FIELD POTENTIAL

Direct calculation of the contact probability $g_{ij}(0)$ is very complicated even in OCP. In principle, it can be done by path integral Monte Carlo (PIMC) simulations, but it requires very large computer resources. PIMC calculations performed so far are limited to a small number of plasma ions (current OCP results are described in Refs. [24–26]). In BIMs one needs a larger number of ions, N_1 and N_2, to achieve good accuracy.

We will use a simple mean-field model, summarized in this section. It can be treated as a first approximation to the PIMC approach [27]. Previously we showed [17] that it is in good agreement with the PIMC calculations of Militzer and Pollock [26] for OCP.

A classical pair correlation function, calculated by the classical Monte Carlo (MC) method, can be presented as

$$g_{ij}^{\rm MC}(r) = \exp\left[\frac{1}{k_B T}\left(\frac{Z_i Z_j e^2}{r} - H_{ij}(r)\right)\right], \tag{13}$$

where $H_{ij}(r)$ is the mean-field potential to be determined.

The Taylor expansion of $H_{ij}(r)$ in terms of r for a strongly coupled ion system should contain only even powers [28]. The first two terms can be derived analytically in the same technique as proposed by Jancovici [29] for OCP. The mean-field potential at low $r \ll a_{ij}$ takes the form [30]

$$H_{ij}(r) \approx k_B T h_{ij}^0 - \frac{Z_i Z_j e^2}{2 a_{ij}^{\rm comp}}\left(\frac{r}{a_{ij}^{\rm comp}}\right)^2, \tag{14}$$

where

$$h_{ij}^0 = f_0(\Gamma_i) + f_0(\Gamma_j) - f_0\left(\Gamma_{ij}^{\rm comp}\right), \tag{15}$$

and $f_0(\Gamma)$ is the Coulomb free energy per ion in OCP. Here, the linear mixing rule is assumed. In principle, h_{ij}^0 can be extrapolated from MC $H_{ij}(r)$ data (e.g., Ref. [31]), but the problem is delicate [32], and we expect that using the linear mixing rule is preferable. The linear mixing rule has been confirmed with high accuracy [33,34], but its uncertainties have been the subject of debate; see Ref. [35] for recent results.

To determine the mean-field potential in BIMs, we performed extensive MC calculations of $H_{ij}(r)$. We did 129 MC runs. In each run, we calculated pair correlation functions g_{11}, g_{12}, and g_{22} for a given set of the parameters Z_1, Z_2, N_1, N_2, and Γ_1. In Fig. 2, each set is shown by a symbol, as indicated in the legends. The top panel demonstrates a fraction of particles 2, x_2, versus Γ_1 for different ratios of Z_2/Z_1. In the bottom panel, we show the Z_2/Z_1 ratio versus Γ_1 for different values of x_2. For some parameter sets (e.g., for $\Gamma_1 = 180$, $x_2 \approx 0.05$, $Z_2/Z_1 = 4/3$), we conducted a number of MC runs with different initial configurations (random or regular lattice) and/or different simulation times. We did not find any significant dependence of the mean-field potential (for $r < 2a_{ij}$) on the initial parameters. From all our simulations, we extracted $H_{11}(r)$, $H_{12}(r)$, and $H_{22}(r)$ and removed some low-r points with large MC noise. We then fit these functions at $r \lesssim 2a_{ij}$ by the simple universal analytical expression

$$H_{ij}(r) = k_B T \Gamma_{ij}^{\rm eff} \times \sqrt{\frac{U_0^2 + U_1 x^4 + U_2 x^8}{1 + U_3 x + U_4 x^2 + U_5 x^4 + U_6 x^6 + U_2 x^{10}}}, \tag{16}$$

where $x = r/a_{ij}^{\rm eff}$, $U_0 = h_{ij}^0/\Gamma_{ij}^{\rm eff}$, $U_1 = 0.0319$, $U_2 = 0.0024$, $U_3 = 0.22\,(\Gamma_{ij}^{\rm eff})^{-0.7}$, $U_4 = 2^{-1/3}(a_{ij}^{\rm eff}/a_{ij}^{\rm comp})^2/U_0$, $U_5 = 0.111$, and $U_6 = 0.0305$. Note that U_0 and U_4 are fixed by the low-r asymptote of $H_{ij}(r)$ at strong Coulomb coupling, $\Gamma_{ij} \gg 1$, Eq. (14). For a better determination of $H_{12}(r)$, we introduce the effective ion sphere radius $a_{ij}^{\rm eff}$ and the Coulomb

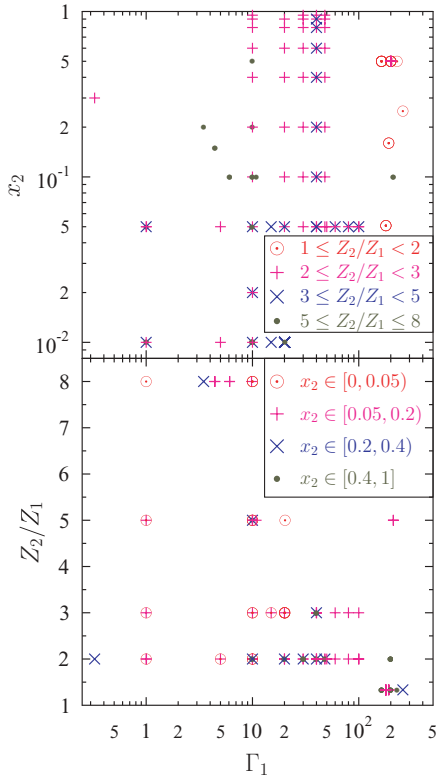

FIG. 2. (Color online) Every BIM MC run is shown on both panels. Top: x_2 vs Γ_1 for runs with different ratios of Z_2/Z_1 as indicated in the legend. Bottom: Z_2/Z_1 vs Γ_1 for runs with different fractions x_2, see legend.

coupling parameter Γ_{ij}^{eff}:

$$a_{ij}^{\text{eff}} = \left(\frac{a_i^p + a_j^p}{2}\right)^{1/p}, \quad \Gamma_{ij}^{\text{eff}} = \frac{Z_i Z_j e^2}{k_B T a_{ij}^{\text{eff}}}. \tag{17}$$

Here, p is an additional fit parameter, which is found to be $p = 1.6$. Note that $a_{ii}^{\text{eff}} = a_{ii} = a_i$ for reactions with identical nuclei ($i = j$). If, however, $i \neq j$ the parameters a_{ij}^{eff} and a_{ij} differ by a few percent, and this difference is very important. Using a_{ij} to define x in Eq. (16) and using $H_{ij}(r)$ to reproduce the pair correlation function $g_{ij}(r)$ through Eq. (13), we find the first peak of g_{ij} to be unrealistically deformed for large $Z_2/Z_1 \gtrsim 5$.

Let us mention that in the OCP case, our fit expression (16) is not the same as the one we used previously [17]. Equation (16) seems to be better, because it better describes the first peak of $g(r) = g_{ii}(r)$, especially at very large $\Gamma \gtrsim 200$. For a OCP at $\Gamma \lesssim 200$, the old and new fit expressions give approximately the same accuracy of $H(r) = H_{ii}(r)$.

Four examples of MC runs are shown in Fig. 3. For each run (on each plot) we show the dimensionless mean-field potential $u_{ij} = H_{ij}(r)/(k_B T \Gamma_{ij})$ vs r/a_e. Solid lines are MC data, dashed lines are derived from the fit expression (16). One can see numerical noise of MC data at low r; it is especially strong in the lowest plot for $\Gamma_e = 5$. During the fitting procedure, we removed some low-r points with high MC noise. Our fitting ranges are shown by pairs of thin dotted lines

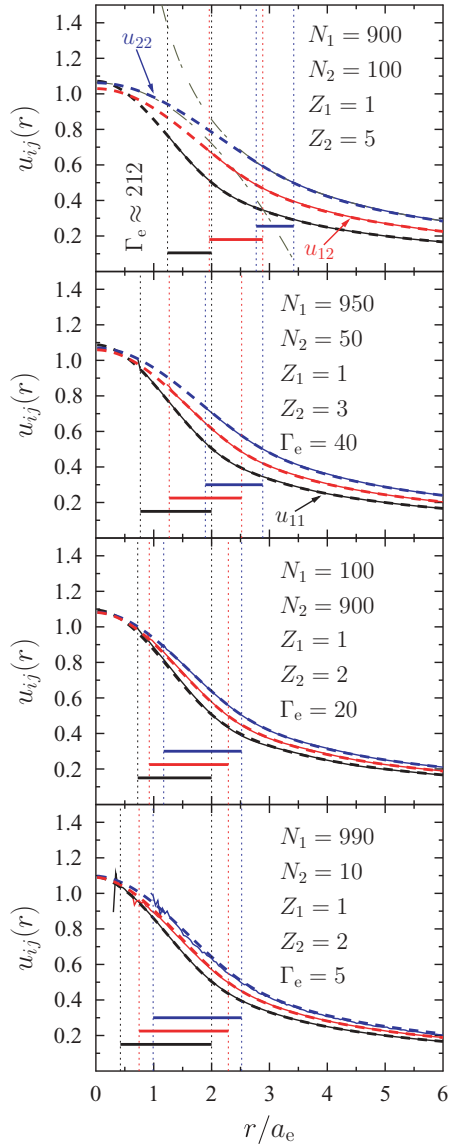

FIG. 3. (Color online) Mean-field potential u_{ij} vs r/a_e for four MC runs. Solid lines are extracted from MC data, dashed lines are given by the fit in Eq. (16). On each plot, the lines that are upper at $r \gtrsim 2\,a_e$ correspond to $u_{22}(r)$; lower lines are u_{12}, and lowest lines give u_{11}. Thin vertical dotted lines connected by thick solid lines show the ranges of r used in the fitting.

connected by a thick solid line. The low-r bound of the fitting region is different for H_{11}, H_{12}, and H_{22} and for each MC run. The high-r bound was taken to be $2a_{ij}$ for all data. Thus, all our fits include the vicinity of the first peak of a pair correlation function at $r \sim 1.8a_{ij}$. Although we have no MC data at low r, we expect that our approximation is well established because it satisfies the accurate low-r asymptote (14). Also, it satisfies the large-r asymptote $u_{ij}(r \to 1) = a_{ij}/r$, which corresponds to the fully screened Coulomb potential. Both asymptotes for u_{22} are shown on the upper plot by dash-dot lines. One can see that they nicely constrain the mean-field potential.

Poor MC statistics at low r can be, in principle, increased using specific MC schemes [36], but this is beyond the scope of the present paper.

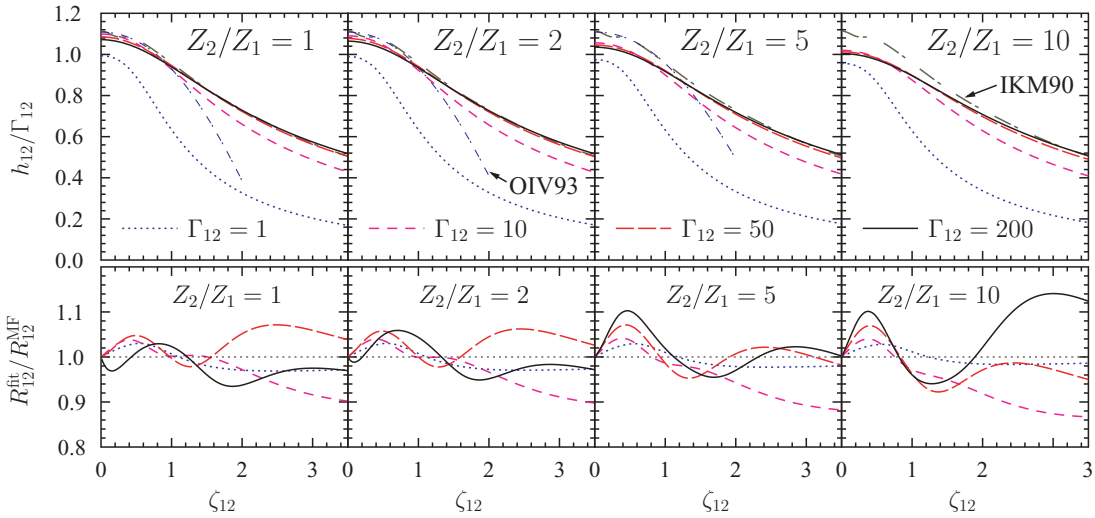

FIG. 4. (Color online) Top: Enhancement factors h_{12}/Γ_{12} for several Γ_{12} and Z_2/Z_1 (shown on each panel). The long-dash-dot line presents the fit expression by Itoh *et al.* [23] (IKM90); the short-dash-dot lines are the results by Ogata *et al.* [37] (OIV93), calculated for $\Gamma_{12} = 50$, as an example (the latter lines are shown only for $\zeta_{12} < 2$ and $Z_2/Z_1 \leqslant 5$ which are the fit bounds in OIV93). Bottom: Ratios of $R_{12}^{\rm fit}$, given by Eq. (23), to the mean-field reaction rate $R_{12}^{\rm MF}$, given by Eq. (20), vs ζ_{12}. See text for details.

Previously the mean-field approximation was used by Itoh *et al.* [23] and Ogata *et al.* [37]. While we use the correct form of the linear mixing rule [Eq. (15)] to calculate $u_{12}(0)$, the cited authors restricted themselves by OCP results, which depend only on Γ_{12} (but not on Z_2/Z_1). The results of this simplification are discussed in Sec. IV; they are visible in Fig. 4. In addition, our approximation is based on a more representative set of MC runs (see Fig. 2), and each run was done with better accuracy. For example, there is no visible $g_{ij}(r)$ noise in the vicinity of the first peak in our data, whereas this noise is obvious in Fig. 1 of Ref. [37]. We have also checked that our approximation (16) better reproduces all our MC data than approximations of both groups [23,37]. As noted by Ogata *et al.* [37], the height of the first $g_{ij}(r)$ peak depends on the fraction of ions with larger charge (the peaks become higher as this fraction increases). Our data confirm this statement for a not very large Coulomb coupling parameter, $\Gamma_1 \lesssim 10$. Ogata *et al.* [37] added a correction for this feature in their approximation of u_{11}. It helps describe the first $g_{11}(r)$ peak for some of our runs (e.g., for $\Gamma_1 = 10$, $Z_2/Z_1 = 5$, and $x_2 = 0.2$). However, we think that we still do not have enough data to quantitatively describe this correction to the linear mixing with good accuracy, and we use the mean-field potential of Eq. (16) based on the linear mixing rule throughout the paper. In the Appendix we describe the corrections to the linear mixing on a phenomenological level.

IV. ENHANCEMENT OF NUCLEAR REACTION RATES

Let us introduce the enhancement factor $F_{ij}^{\rm scr}$ of a nuclear reaction rate $R_{ij}^{\rm scr}$ under the effect of plasma screening,

$$R_{ij}^{\rm scr} = R_{ij}^{\rm th}\, F_{ij}^{\rm scr}, \quad F_{ij}^{\rm scr} = \exp(h_{ij}). \tag{18}$$

Here, $R_{ij}^{\rm th}$ is the reaction rate in the absence of the screening. In can be calculated using the classical theory of thermonuclear burning,

$$R_{ij}^{\rm th} = \frac{4 n_i n_j}{1+\delta_{ij}} \frac{S_{ij}\left(E_{ij}^{\rm pk}\right)}{k_B T} \sqrt{\frac{2E_{ij}^{\rm pk}}{3\mu_{ij}}} \exp(-\tau_{ij}). \tag{19}$$

The barrier penetrability parameter τ_{ij} and the Gamow-peak energy $E_{ij}^{\rm pk}$, which enter this equation, are defined, respectively, by Eqs. (10) and (11).

Using $H_{ij}(r)$, we can calculate the reaction rate. This calculation takes into account the plasma screening enhancement in the mean-field approximation (as was done for OCP in our previous paper [17]),

$$R_{ij}^{\rm MF} = \frac{n_i\, n_j S_{ij}\left(E_{ij}^{\rm pk'}\right)}{1+\delta_{ij}} \sqrt{\frac{8}{\pi \mu_{ij} (k_B T)^3}} \times \int_{E_{\rm min}}^{\infty} dE\, \exp\left[-\frac{E}{k_B T} - P_{ij}(E)\right]. \tag{20}$$

Here, E is the center-of-mass energy of the colliding nuclei (with a minimum value $E_{\rm min}$ at the bottom of the potential well), $\exp(-E/k_B T)$ comes from the Maxwellian energy distribution of the nuclei, and

$$P_{ij}(E) = \frac{2\sqrt{2\mu_{ij}}}{\hbar} \int_0^{r_t} dr \sqrt{\frac{Z_i Z_j e^2}{r} - H_{ij}(r) - E} \tag{21}$$

is the Coulomb barrier penetrability (r_t being a classical turning point).

In the WKB mean-field approximation, the enhancement factor of the nuclear reaction rate is

$$F_{ij}^{\rm scr} = R_{ij}^{\rm MF}\{H_{ij}\} / R_{ij}^{\rm MF}\{H_{ij} = 0\}. \tag{22}$$

In the cases of physical interest, $R_{ij}^{\rm MF}\{0\}$ can be integrated by the saddle-point method. However, we always integrate numerically in Eq. (20).

The calculated enhancement factor $F_{ij}^{\rm scr}$ can be fitted as

$$\log F_{ij}^{\rm scr} = f_0\left(\frac{\Gamma_i}{\tau_{ij}}\right) + f_0\left(\frac{\Gamma_j}{\tau_{ij}}\right) - f_0\left(\frac{\Gamma_{ij}^{\rm comp}}{\tau_{ij}}\right), \qquad (23)$$

where $f_0(\Gamma)$ is a free energy per ion in a OCP. We use the most accurate available analytic fit for $f_0(\Gamma)$ suggested by Potekhin and Chabrier [38]:

$$\begin{aligned} f_0(\Gamma) = A_1[&\sqrt{\Gamma\,(A_2+\Gamma)} \\ &- A_2\ln(\sqrt{\Gamma/A_2}+\sqrt{1+\Gamma/A_2})] \\ &+ 2A_3[\sqrt{\Gamma} - \arctan(\sqrt{\Gamma})] \\ &+ B_1\left[\Gamma - B_2\ln\left(1+\frac{\Gamma}{B_2}\right)\right] \\ &+ \frac{B_3}{2}\ln\left(1+\frac{\Gamma^2}{B_4}\right). \end{aligned} \qquad (24)$$

Here, $A_1 = -0.907$, $A_2 = 0.62954$, $A_3 = -\sqrt{3}/2 - A_1/\sqrt{A_2} \approx 0.2771$, $B_1 = 0.00456$, $B_2 = 211.6$, $B_3 = -10^{-4}$, and $B_4 = 0.00462$. We also introduce a number of additional parameters:

$$\begin{aligned} &y_{ij} = \frac{4\,Z_i\,Z_j}{(Z_i+Z_j)^2}, \quad c_1 = 0.013\,y_{ij}^2, \\ &c_2 = 0.406\,y_{ij}^{0.14}, \quad c_3 = 0.062\,y_{ij}^{0.19} + 1.8/\,\Gamma_{ij}, \\ &t_{ij} = \left(1 + c_1\,\zeta_{ij} + c_2\,\zeta_{ij}^2 + c_3\zeta_{ij}^3\right)^{1/3}. \end{aligned} \qquad (25)$$

The rms relative error of the fit of $F_{\rm scr}$ is 5%. The maximum error ~14% occurs at $\zeta_{ij} \approx 4.8$, $\Gamma_{12} \approx 25$, and $Z_2/Z_1 \approx 10$. The fit was constructed for $1 \leqslant Z_2/Z_1 \leqslant 10$, $1 \leqslant \Gamma_{12} \leqslant 200$ (we also used $\Gamma_{12} = 400$ and 600 for testing), and $\zeta_{12} \leqslant 8$ (larger values of ζ_{12} were not included into fitting but used for tests). As for OCP in our previous paper [17], at larger Γ the relative errors increase.

In the limit of $\zeta_{ij} \to 0$, we have $\log F_{ij}^{\rm scr} = h_{ij}^0$. This is the well-known relation (e.g., see Refs. [39,40]); its formal proof is given in Ref. [41].

Our fit formula (23) has the same form as the thermodynamic relation (15), but it contains Coulomb coupling parameters Γ_{ij} divided by τ_{ij}. It generalizes our OCP result [17].

Figure 4 shows the normalized enhancement factor $h_{12}/\,\Gamma_{12}$ (bottom panels) as a function of ζ_{12} for $\Gamma_{12} = 1, 10, 50$, and 200 and $Z_2/Z_1 = 1, 2, 5$, and 10. The first panel (for $Z_2 = Z_1$) corresponds not only to a reaction in OCP but also to reactions of identical nuclei in a mixture; the mean-field potential and the plasma screening enhancement do not depend on an admixture of other elements [see Eqs. (16) and (23)], as long as the Coulomb coupling parameter is not too small, $\Gamma_{ij} \gtrsim 1$, and the linear mixing is valid. The larger the Γ_{ij}, the weaker the dependence of $h_{12}/\,\Gamma_{12}$ on Γ_{ij}. Long-dashed lines, plotted for $\Gamma_{12} = 50$, significantly differ from dashed lines which are for $\Gamma_{12} = 10$, but can be hardly distinguished from solid lines, plotted for $\Gamma_{12} = 200$. Therefore, the total enhancement factor $\exp(h_{12})$ depends exponentially on Γ_{12} in the first approximation. The normalized enhancement factor $h_{12}/\,\Gamma_{12}$ suggested by Itoh *et al.* [23] (IKM90) is shown by long-dash-dot lines. It is independent of Γ_{12}, and we show one line in each plot. The short-dash-dot lines demonstrate the fit expression of Ogata *et al.* [37] (OIV93) (for $\Gamma_{12} = 50$ as an example). The lines are cut at $\zeta_{12} = 2$ (which bounds the fit validity). We show no OIV93 line on the panel for $Z_2/Z_1 = 10$ because there are no OIV93 simulations for such large Z_2/Z_1 ratios. The two lines, IKM90 and OIV93, demonstrate higher enhancement, especially for $\zeta_{12} \lesssim 1$ and large Z_2/Z_1. First, the IKM90 and OIV93 simulations used less accurate thermodynamic approximations for calculating $u_{ij}(0)$. For large Z_2/Z_1 ratios, their fit error increases because of the use of the OCP expression (dependent only on Γ_{12}, but not on Z_2/Z_1) for determining $u_{ij}(0)$. This increases the difference between our and their approximations at large Z_2/Z_1 (see also a discussion in Sec. IIIC of Ref. [16]). IKM90 and our ζ_{12} dependence of the enhancement factors is qualitatively the same, but the results of OIV93 (and of the preceding paper [30]) are qualitatively different. As we showed previously [17], such results contradict recent PIMC results by Militzer and Pollock [26] for OCP. The deviation of the IKM90 enhancement factors at low ζ_{ij} values comes possibly from using an oversimplified mean-field potential.

The indicated differences between IKM90, OIV93, and our results can lead to very large differences of the total enhancement factor $\exp(h_{12})$. For example, at $Z_2/Z_1 = 5$ and $\Gamma_{12} = 200$ the difference can reach five orders of magnitude. Accordingly, we do not present the IKM90 and OIV93 results in the lower panels of Fig. 4, which give the ratio of the reaction rates $R_{12}^{\rm fit}$, given by the fit expression (23), to the reaction rate $R_{12}^{\rm MF}$, calculated in the mean-field approximation using Eq. (20). The very small difference ($\lesssim$10%) shown on these plots is true only by adopting the mean-field potential [Eq. (16)]. The uncertainties of the reaction rates, which come from the uncertainties of the mean-field potential and inaccuracy of the mean-field approximation, can be larger.

Let us stress that Eq. (23) is derived for the case of strong screening; it is invalid at $\Gamma_{12} \lesssim 1$, where the adopted linear mixing rule fails. A simple correction of the enhancement factor for weaker screening is suggested in the Appendix. It allows us to extend the results for the case of weaker Coulomb coupling.

V. ASTROPHYSICAL *S* FACTORS: GAMOW-PEAK ENERGIES AT STRONG SCREENING

In the previous section, we focused on the plasma screening of the Coulomb barrier penetration in a dense plasma environment. Now we discuss the effects of plasma screening on the astrophysical *S* factor, which describes the nuclear interaction of the reacting nuclei after the Coulomb barrier penetration. The latter effects are not expected to be very strong because of the not too strong energy dependence of $S_{ij}(E)$ (see, e.g., Ref. [42]), but we consider them for completeness.

The astrophysical *S* factor describes the effects of short-range nuclear forces, and it should depend on the parameters of the reacting nuclei just before a reaction event. The energy $E_{ij}^{\rm pk'}$ substituted into $S(E)$ in Eq. (20) should be corrected for the mean-field potential created by other ions, $E_{ij}^{\rm pk'} = E + H_{ij}(0)$.

This correction is obvious and has been used in calculations (e.g., in Ref. [43]), but its formal proof has not been published, to the best of our knowledge. The reaction rate in the presence of plasma screening can be calculated as

$$R_{ij} = \frac{n_i n_j}{1+\delta_{ij}} \left(\frac{8}{\pi \mu_{ij} T^3}\right)^{1/2} \int \widetilde{\sigma}_{ij}(E) E \exp\left(-\frac{E}{T}\right) dE, \tag{26}$$

where $\widetilde{\sigma}_{ij}(E)$ is the reaction cross section including the screening effects. To calculate R_{ij}, let us recall that the barrier penetration model with a parameter-free model of nuclear interaction gives a good description of reaction cross sections [15]. In the absence of plasma screening at not too high energies E (where only the s-wave channel is important), this model reduces to the WKB calculation of the penetrability through a potential that is the sum of the Coulomb potential and the potential $V_{ij}^N(r, v_{ij}^2)$, which describes the short-range nuclear interaction. The latter potential depends on the local relative velocity $v(r, E)$ of the reactants given by

$$v^2 = \frac{2}{\mu_{ij}} \left[E + H_{ij}(r) - \frac{Z_i Z_j e^2}{r} - V_{ij}^N(r, v^2)\right]. \tag{27}$$

Let us generalize this model by adding the screening potential $H_{ij}(r)$ and write the cross section as

$$\widetilde{\sigma}_{ij}(E) = \frac{\pi}{k_{ij}^2} \exp\left[-\frac{2\sqrt{2\mu_{ij}}}{\hbar} \int_{r_{\rm tn}}^{r_{\rm t}} dr \times \sqrt{\frac{Z_i Z_j e^2}{r} - H_{ij}(r) + V_{ij}^N(r, v_{ij}^2) - E}\right]. \tag{28}$$

Here, $r_{\rm tn}$ and $r_{\rm t}$ are classical turning points and $k_{ij}^2 = 2\mu_{ij} E/\hbar^2$. Substituting this equation into Eq. (26), we have

$$R = \frac{n_i n_j}{1+\delta_{ij}} \left(\frac{8}{\pi \mu_{ij} T^3}\right)^{1/2} \times \int \widetilde{S}_{ij}(E) \exp\left[-\frac{E}{T} - P_{ij}(E)\right] dE, \tag{29}$$

where $\widetilde{S}_{ij}(E)$ is the astrophysical factor calculated in the presence of the plasma screening

$$\widetilde{S}_{ij}(E) = \widetilde{\sigma}_{ij} E \exp\left[P_{ij}(E)\right]; \tag{30}$$

$P_{ij}(E)$ is defined by Eq. (21). The potential $V_{ij}^N(r, v)$ is nonzero only for very small $r \lesssim r_N$. Let us substitute Eqs. (21) and (28) into (30) and divide all integrals into two parts, at $r < r_N$ and $r \geqslant r_N$. The integrals over $r > r_N$ which come from $P_{ij}(E)$ and $\widetilde{\sigma}_{ij}(E)$ will be exactly the same [$V_{ij}^N(r, v) = 0$ for $r > r_N$] and cancel each other. As a result,

$$\widetilde{S}_{ij}(E) = \frac{\pi\hbar^2}{2\mu_{ij}} \exp\left\{\frac{2\sqrt{2\mu_{ij}}}{\hbar} \times \left[\int_0^{r_N} \sqrt{\frac{Z_i Z_j e^2}{r} - H_{ij}(r) - E} dr - \int_{r_{\rm tn}}^{r_N} \sqrt{\frac{Z_i Z_j e^2}{r} - H_{ij}(r) + V_{ij}^N(r, v^2) - E}\, dr\right]\right\}. \tag{31}$$

As expected, the astrophysical S factor is determined by the behavior of the total potential $Z_i Z_j e^2/r - H_{ij}(r) + V_{ij}^N(r, v^2)$ in the low-r region $r < r_N$, where the nuclear forces are important. Because r_N is much smaller than the ion sphere radius a_{ij}, which is a typical length scale of $H_{ij}(r)$ (e.g., Fig. 3), we can neglect variations of $H_{ij}(r)$ for $r < r_N$ and replace $H_{ij}(r)$ under the integrals in Eq. (31) by $H_{ij}(0)$. The $S_{ij}(E)$ factor in the absence of plasma screening is given by the same Eq. (31) but at $H_{ij}(r) = 0$. Thus, $\widetilde{S}_{ij}(E)$ is defined by the same equation as $S_{ij}(E')$, provided $E' = E + H_{ij}(0)$. In other words, $\widetilde{S}_{ij}(E) = S_{ij}(E + H_{ij}(0))$, and the reaction rate is

$$R = \frac{n_i n_j}{1+\delta_{ij}} \left(\frac{8}{\pi \mu_{ij} k_B{}^3 T^3}\right)^{1/2} \times \int S_{ij}(E + H_{ij}(0)) \exp\left[-\frac{E}{k_B T} - P_{ij}(E)\right] dE. \tag{32}$$

If this simple barrier penetration theory were invalid and the hypothesis of low-energy hindrance of nuclear reactions [44] were correct, such a simple correction of astrophysical S factors for the plasma screening effects could be insufficient, and the calculation of the reaction rate would be much more complicated. We will not consider this possibility.

As in the absence of the plasma screening, the main contribution to the integral (32) comes from a narrow energy range. We neglect the energy dependence of $S_{ij}(E + H_{ij}(0))$ in this range and take the S factor out of the integral. The contact probability in the mean-field model is given by

$$g_{ij}(0) = \frac{2\sqrt{2\pi\mu_{ij}}}{k_B{}^{3/2} T^{3/2}} \frac{Z_1 Z_2 e^2}{\hbar} \int \exp\left[-\frac{E}{k_B T} - P_{ij}(E)\right] dE, \tag{33}$$

so that the reaction rate reads

$$R_{ij} = \frac{2 n_i n_j}{1+\delta_{ij}} \frac{a_{ij}^B}{\hbar\pi} S_{ij}\left(E_{ij}^{\rm pk} + H_{ij}(0)\right) g_{ij}(0). \tag{34}$$

We have calculated the modified Gamow-peak energy $E_{ij}^{\rm pk'} = E_{ij}^{\rm pk} + H_{ij}(0)$, which should be used as an argument of S factors, in a wide range of plasma parameters. It can be fitted as

$$E_{ij}^{\rm pk'} = \left[H_{ij}^3(0) + \left(k_B T \frac{\Gamma_{ij}}{\zeta_{ij}}\right)^3\right]^{1/3}. \tag{35}$$

The maximum relative fit error for $1 \leqslant \Gamma_{ij} \leqslant 200$, $\zeta_{ij} \leqslant 8$, and $0.1 \leqslant Z_i/Z_j \leqslant 10$ is 4%. It takes place at $\Gamma_{ij} = 1$, $\zeta_{ij} = 1$, and $Z_i = Z_j$. Because of large nuclear physics uncertainties in

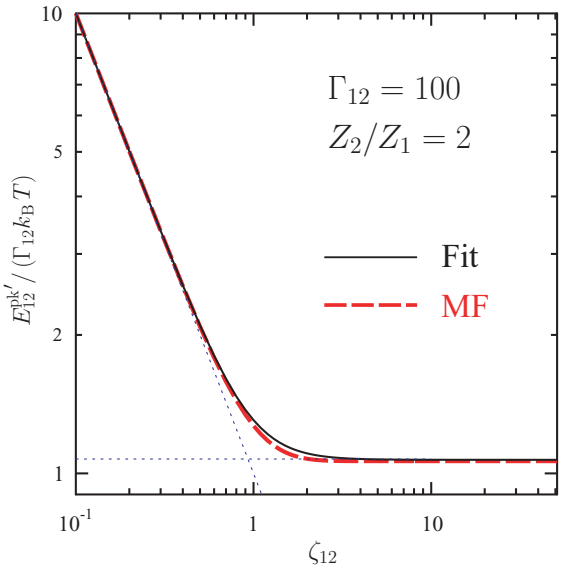

FIG. 5. (Color online) Gamow-peak energy $E_{ij}^{pk'}$ normalized for Γ_{12} as function of ζ_{12} at $Z_2/Z_1 = 2$ and $\Gamma_{12} = 100$. Solid line is the fit expression (35), dashed line shows the mean-field result. Thin dotted lines correspond to the low-ζ_{ij} thermonuclear asymptote $E_{ij}^{pk'} = \Gamma_{12}/\zeta_{12}$ and high-ζ_{ij} pycnonuclear asymptote $E_{ij}^{pk'} = H_{ij}(0)$. See text for details.

our knowledge of $S(E)$ at the low energies of astrophysical interest, this accuracy is more than sufficient. An example of the dependence of $E_{12}^{pk'}/\Gamma_{12}$ on ζ_{12} is shown in Fig. 5 for $Z_2/Z_1 = 2$ and $\Gamma_{12} = 100$. The solid line is the fit (35), the dashed line is a result of the exact $E_{ij}^{pk'}$ calculation in the mean-field model. The peak energy $E_{ij}^{pk'}$ has two asymptotes shown by thin dotted lines. At low $\zeta \ll 1$, the reaction occurs in the thermonuclear regime, $E_{ij}^{pk'} = \Gamma_{ij}/\zeta_{ij}$, which is the standard classical result. For large $\zeta_{ij} \gg 1$, we have $E_{ij}^{pk'} \to H_{ij}(0)$. The classical asymptote $E_{ij}^{pk'} = \Gamma_{ij}/\zeta_{ij}$ is applicable at $\zeta_{ij} \lesssim 0.5$, where the plasma screening enhancement can be very strong (tenths orders of magnitude). This is because in the thermonuclear regime, the tunneling length is not very large and $H_{ij}(r)$ does not significantly change it (see Fig. 6); ions tunnel through the Coulomb potential, shifted by $H_{ij}(0)$. The shift increases the probability of close ion collisions by a factor of $\exp(H_{ij}(0)/T)$, but does not change the Maxwellian energy distribution and the dependence of the tunneling probability on tunneling length. As a result, the main contribution to the reaction rate comes from ions with the same tunneling length (and the same $E_{ij}^{pk'}$), as in the absence of plasma screening.

The large-ζ_{ij} asymptote is simple. For such parameters, thermal effects are small and the ions, which mainly contribute to the reaction rate, correspond to the minimum energy of the total potential $Z_1Z_2/r + H_{ij}(r)$. This energy is small compared with $H_{ij}(0)$, so $E_{ij}^{pk'} \approx H_{ij}(0)$. One can see a small difference of $H_{ij}(0)$, shown by the thin dotted line in Fig. 5, and the asymptote of $H_{ij}(0)$ at large ζ_{ij}. This difference does not introduce significant uncertainties to the reaction rate because of much larger nuclear-physics uncertainties caused by our poor knowledge of $S(E)$ at low energies (e.g., Ref. [16]). We assume that the $E_{ij}^{pk'}$ approximation (35) is valid (at least qualitatively) not only for thermonuclear burning with strong screening but also for pycnonuclear burning. In the pycnonuclear regime, the ions occupy their ground states and oscillate near their lattice sites. The reaction rates are determined by zero-point vibrations of the ions. The energy of zero-point vibrations is typically small compared to the minimum energy of the potential $Z_iZ_j/r + \widetilde{H}_{ij}(\boldsymbol{r})$; the latter is much lower than $\widetilde{H}_{ij}(0)$, where $\widetilde{H}_{ij}(\boldsymbol{r})$ is an anisotropic effective potential created by neighboring ions. Therefore, the ions start with a small kinetic energy [the minimum of the $Z_iZ_j/r + \widetilde{H}_{ij}(\boldsymbol{r})$] and tunnel to $r \to 0$ through the Coulomb potential plus the $\widetilde{H}_{ij}(\boldsymbol{r})$. During tunneling, they fall into the potential well $\widetilde{H}_{ij}(\boldsymbol{r})$, and their energy increases by $\widetilde{H}_{ij}(0)$. Therefore, $E_{ij}^{pk'}$ should be equal to $\widetilde{H}_{ij}(0)$, but not to the energy of zero-point vibrations, as assumed in Refs. [14,16,22]. Note that in the relaxed-lattice approximation, $\widetilde{H}_{ij}(0) = H_{ij}(0)$ [14,22].

For example, let us consider E_{ij}^{pk} and the characteristic (half-maximum) energy widths of the Gamow-peak for a ^{12}C and ^{16}O mixture (with equal number densities of C and O ions) at $\rho = 5 \times 10^9$ g cm^{-3}. In Fig. 6, we show the effective total radial mean-field Coulomb potentials $U_{ij}(r) = Z_iZ_je^2/r - H_{ij}(r)(i, j = {}^{12}\text{C}$ or $^{16}\text{O})$ for five temperatures, $T = 10^9, 10^{8.5}, 10^8, 10^{7.5}$, and 10^7 K. For this mixture, the ion-sphere radius of ^{12}C ions is $a_C = 98$ fm, and it is $a_O = 108$ fm for ^{16}O ions. The solid, dotted, and long-dash lines show the CC, CO, and OO potentials, respectively. Each potential $U_{ij}(r)$ has a minimum at $r_{ij} \approx 2a_{ij}$ due to the Coulomb coupling. The thin horizontal lines connected by double-arrow lines in Fig. 6 show the Gamow-peak energy ranges. The types of thin lines are the same as for $U_{ij}(r)$. Thick sections of short horizontal lines, which intersect double-arrow lines, demonstrate the Gamow-peak energies E_{ij}^{pk}. Thick parts of short-dashed lines at small $r < 100$ fm indicate the thermal energy level k_BT measured from the bottom of $U_{ij}(r)$.

The top right panel marked "without screening" shows the same lines (as other panels) for $T = 10^8$ K but neglecting plasma screening. Dramatic difference of unscreened and screened potentials and corresponding Gamow-peak regions is obvious from comparison with the bottom panels. The plasma screening reduces the Gamow-peak energy E_{ij}^{pk} by a factor of 4, but (as described above) does not affect significantly the Gamow-peak width.

Let us discuss Fig. 6 in more detail. The panels plotted for $T = 10^{8.5}$ and 10^9 K (top left and top center, respectively) refer to the thermonuclear reaction regime with strong plasma screening. The next two panels (right bottom and center bottom) are for a colder plasma ($T = 10^8$ K and $T = 10^{7.5}$ K, respectively), while the last (left bottom) panel is for a very cold plasma ($T = 10^7$ K) (that is certainly in the zero-temperature pycnonuclear regime). When the temperature decreases, the Gamow-peak energy range becomes thinner (note the difference of energy scales in different panels) and shrinks to lower energies. If $T \gtrsim 10^8$ K, the Gamow-peak range is still at $E > 0$ [belonging to continuum states in a potential $U_{ij}(r)$], and the peak energy E_{ij}^{pk} (the short-dash horizontal line) is in

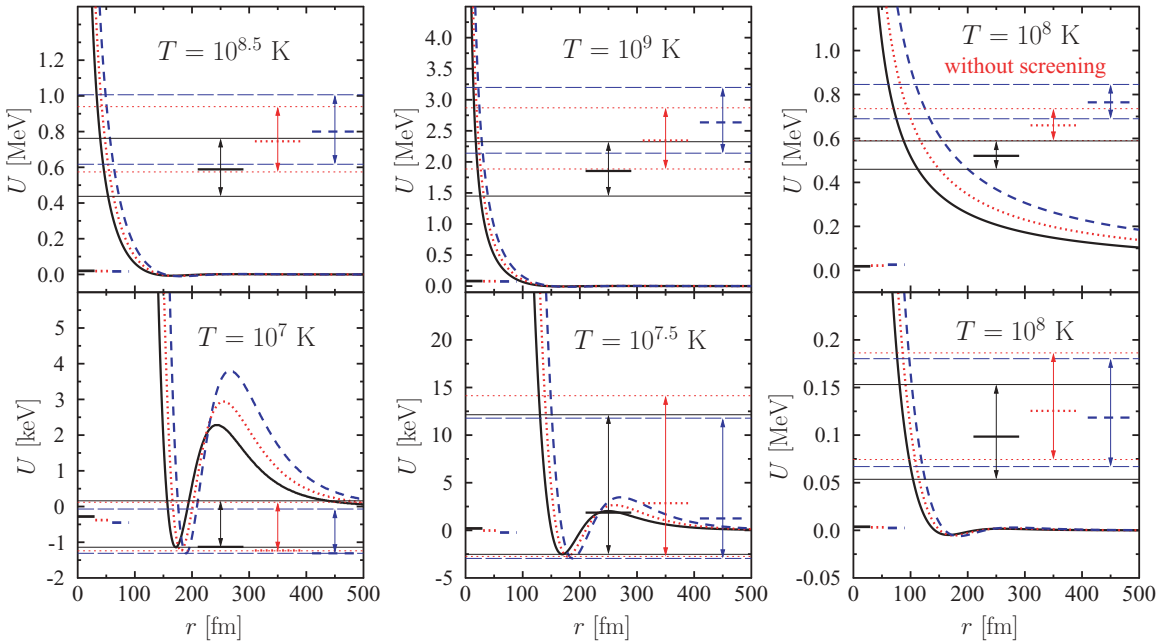

FIG. 6. (Color online) Effective mean-field Coulomb potentials $U_{ij}(r)$ for the reactions $^{12}C + {}^{12}C$ (solid line), $^{12}C + {}^{16}O$ (dotted line), and $^{16}O + {}^{16}O$ (long-dash line) in the mixture of ^{12}C and ^{16}O with equal number densities of these nuclei at $\rho = 5 \times 10^9$ g cm^{-3} and the five temperatures indicated.

the center of the Gamow-peak range. The energies within this range are much higher than $k_B T$, supporting the statement that the main contribution to reaction rates at sufficiently high T comes from suprathermal ions. In these cases, the underlying mean-field WKB approximation is expected to be adequate. In the fourth panel ($T = 10^{7.5}$ K), the lowest energies of the Gamow-peak range become negative (drop to bound states) and $E_{ij}^{\rm pk}$ moves from the center to the lower bound of the Gamow-peak range (so that the Gamow peak becomes significantly asymmetric). The mean-field WKB approach based on the spherically symmetric mean-field potential $H_{ij}(r)$ may still be qualitatively correct but becomes quantitatively inaccurate. Note that the $U_{ij}(r)$ potential becomes positive for $r \gtrsim 200$ fm. This feature is determined by the right wing of the first $g_{ij}(r)$ peak, where $g_{ij}(r)$ becomes smaller than unity. This wing is unimportant in the mean-field model; our approximation gives qualitatively correct $U_{ij}(r)$ for $r \gtrsim 2a_{ij}$ [$g_{ij}(r) \to 1$ for $r \to \infty$]. For the lowest temperature in Fig. 6, the Gamow-peak energy range fully shrinks to bound-state energies, and the formal Gamow-peak energy becomes lower than $k_B T$, nearly reaching the lower bound of the Gamow-peak region. The mean-field WKB approximation breaks down at these low temperatures, and the formally calculated $E_{ij}^{\rm pk}$ is inaccurate. Nevertheless, the energy in the argument of the S factor, $E_{ij}^{\rm pk'} = E_{ij}^{\rm pk} + H_{ij}(0) \approx H_{ij}(0)$, is expected to be well defined.

VI. RESULTS AND DISCUSSION

Figure 7 shows the temperature dependence of the three (C+C, C+O, and O+O) reaction rates in a ^{12}C and ^{16}O mixture with equal number density of carbon and oxygen ions at $\rho = 5 \times 10^9$ g cm^{-3}. For each of the three reactions, the lines represent our mean-field calculations (labeled MF), the fit expression (23) (labeled Fit), and calculations neglecting the plasma screening [$H_{ij}(r) = 0$]. The right vertical scale gives the typical carbon burning time $\tau_{\rm CC} = n_{\rm C}/R_{\rm CC}$. The shaded region ($T < 2.5 \times 10^7$ K) corresponds to bound

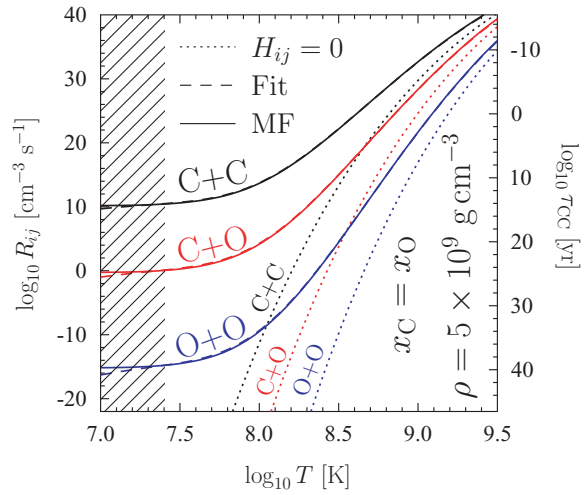

FIG. 7. (Color online) Reaction rates in a $^{12}C + {}^{16}O$ mixture with $x_{\rm C} = x_{\rm O} = 0.5$ at $\rho = 5 \times 10^9$ g cm^{-3}. Solid lines are the mean-field calculations, dashed lines correspond to our fit expression (23), and dotted lines are obtained neglecting the plasma screening. The lines of each type show results for the C+C, C+O, and O+O reactions. The shaded region of $T < 2.5 \times 10^7$ K corresponds to bound Gamow-peak states, $E_{ij}^{\rm pk} < 0$. The right vertical scale shows characteristic carbon burning time $\tau_{\rm CC} = n_{\rm C}/R_{\rm CC}$. See text for details.

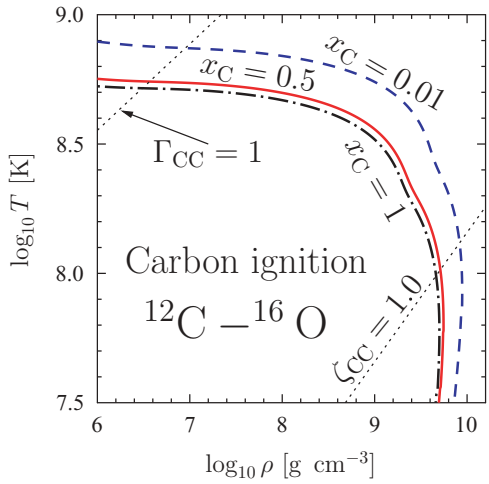

FIG. 8. (Color online) Carbon ignition curve in $^{12}C + ^{16}O$ mixtures. Curves show the mean-field calculations for $x_C = 1, 0.5$, and 0.01. We also plot two thin dotted lines of constant $\Gamma_{CC} = 1$ and $\zeta_{CC} = 1$ to demonstrate typical values of dimensionless parameters. See text for details.

Gamow-peak states (see Fig. 6 and corresponding discussion in the text). This region is similar for all three reactions because of approximately the same charges of reacting ions. For such low temperatures, the mean-field model with isotropic potential is quantitatively invalid but qualitatively correct; the reaction rates become temperature independent, which is the main property of pycnonuclear burning. The pycnonuclear burning rates are rather uncertain [16]; typical rates reported in the literature are one order of magnitude smaller than those extracted from our mean-field calculations at $T \to 0$. The difference may result from the fact that we use the spherically symmetric mean-field potential (rather than more realistic anisotropic potential). In reality, ions can be localized in deeper potential wells near their lattice sites.

The fit and mean-field results, which are mostly indistinguishable in the figure, can strongly differ in the shaded region, especially for the O+O reaction. We do not expect that it is a significant disadvantage of our fit expression (because the mean-field approach becomes invalid at such conditions), but we would like to mention this feature. Note that for the O+O reaction in Fig. 7, the temperature $T = 2.5 \times 10^7$ K corresponds to $\Gamma_{OO} \approx 400$ and the total enhancement factor is $\sim 10^{110}$.

Figure 8 presents carbon ignition curves, which are most important for modeling nuclear explosions of massive white dwarfs (supernova Ia events) and carbon explosions in accreting neutron stars (superbursts). For white dwarfs, it is determined as a line in the T-ρ plane, where the nuclear energy generation rate equals the local neutrino energy losses (which cool the matter). For higher T and ρ (above the curve), the nuclear energy generation exceeds the neutrino losses, and carbon ignites. The curves are plotted for $^{12}C + ^{16}O$ mixtures. The main energy is generated in the C+C reaction even for $x_C = 0.01$, because the C+O and O+O reactions are more strongly suppressed by the Coulomb barrier (see Fig. 7 to compare the reaction rates). In our mean-field model, which employs the linear mixing, the admixture of oxygen affects the C+C burning only by reducing the number density of carbon nuclei [not through the contact probability $g_{CC}(0)$; see Eq. (34)], so the C+C reaction rate is $\propto x_C^2$. The neutrino energy losses are mainly produced by plasmon decay and electron-nucleus bremsstrahlung processes. The neutrino emissivity owing to plasmon decay is calculated using the results of Ref. [45] (with the online table http://www.ioffe.ru/astro/NSG/plasmon/table.dat). The neutrino bremsstrahlung emissivity is calculated using the formalism of Kaminker *et al.* [46], which takes into account electron band structure effects in crystalline matter. For a CO mixture, this neutrino emissivity is determined using the linear mixture rule.

Two thin dotted lines in Fig. 8 correspond to constant $\Gamma_{CC} = 1$ and $\zeta_{CC} = 1$. The other lines are the mean-field calculations for $x_C = 1$ (pure carbon matter), 0.5, and 0.01. For a fixed ρ, the higher x_C, the higher the number density of carbon ions and the higher the reaction rate. This intensifies carbon burning, and the carbon ignites at a lower temperature. For high densities, the carbon ignition curve bends, and the carbon can ignite at very low temperatures. This is caused by a weakening in the temperature dependence of the reaction rate (see Fig. 7) and by a strong suppression of neutrino emission with decreasing temperature.

VII. CONCLUSIONS

We have analyzed the plasma screening enhancement of nuclear reaction rates in binary ionic mixtures. We have used a simple model for the enhancement factor based on the radial WKB tunneling of the reacting nuclei in their Coulomb potential superimposed with the static mean-field potential created by neighboring plasma ions. We have performed accurate Monte Carlo calculations of the mean-field plasma potential for a two-component strongly coupled plasma of ions and proposed a simple and accurate analytic fit to the plasma potential (Sec. III). We have calculated the plasma enhancement factors of nuclear reaction rates in the mean-field WKB approximation and obtained their accurate fit (Sec. IV). We have also analyzed the effect of the plasma screening on astrophysical S factors and Gamow-peak energies (Sec. V). To illustrate the results, we analyzed nuclear burning in $^{12}C + ^{16}O$ mixtures (Sec. VI).

We demonstrate that the mean-field WKB method gives qualitatively correct (temperature independent) reaction rates even in the zero-temperature pycnonuclear burning regime. In this regime, the dynamics of the reacting ions is determined by zero-point vibrations; they fuse along selected (anisotropic) close-approach trajectories [14]; the mean-field radial WKB method was initially expected to be absolutely inadequate. Let us mention in passing that the problem of pycnonuclear burning has not been accurately solved even for OCP plasma (e.g., see Ref. [17]); furthermore, the uncertainties of the solution increase in multicomponent mixtures (see Ref. [16], and references therein).

Other uncertainties in our knowledge of the reaction rates come from nuclear physics. As a rule, the astrophysical S

factors cannot be experimentally measured for such low energies as Gamow-peak energies in stellar matter. For example, the lowest experimental point for the $^{12}C + {}^{12}C$ reaction is $\sim$2.1 MeV, whereas typical Gamow-peak energies $E_{ij}^{pk'}$ are $\sim$1 MeV. Therefore, one needs to extrapolate experimental results to the lowest energies. Throughout the paper we assumed a smooth energy dependence of astrophysical S factors, which is supported by calculations in the frame of the barrier penetration model (e.g., Ref. [42]). However, some models (e.g., that in Ref. [47]), predict resonances at low energy, which can significantly change the reaction rates and ignition curve [48]. We do not discuss such effects in the present paper. New experimental and theoretical studies of astrophysical S factors are needed to solve this problem.

Our results can be used to model various nuclear burning phenomena in dense stellar matter (Sec. I), particularly, in neutron star envelopes and white dwarf cores. Let us mention that neutron stars can possess strong magnetic fields (up to $\sim 10^{15}$ G in highly magnetized neutron stars called magnetars). Strong fields can influence ion motion and plasma screening (which is almost unexplored in the literature). Such effects are expected to be strong when the ion cyclotron frequency exceeds the ion plasma frequency. For the magnetic fields of $\sim 10^{15}$ G, this would take place at densities $\rho \lesssim 10^8$ g cm^{-3} (in a thin layer, not deeper than 10 m under the neutron star surface). Nuclear burning at these densities deserves further study.

ACKNOWLEDGMENTS

We are grateful to D.G. Yakovlev for useful remarks. The work of AIC was partly supported by the Russian Foundation for Basic Research (Grant 08-02-00837) and by the State Program "Leading Scientific Schools of Russian Federation" (Grant NSh 2600.2008.2). The work of HED was performed under the auspices of the US Department of Energy at the Lawrence Livermore National Laboratory under Contract No. W-7405-ENG-48.

APPENDIX: CORRECTION OF ENHANCEMENT FACTORS FOR WEAK NONIDEALITY

Our fit expression (23) does not reproduce the well-known Debye-Hückel enhancement factor for weak Coulomb coupling ($\Gamma_{ij} \ll 1$),

$$h_{ij}^{DH} = 3^{1/2} Z_i\, Z_j \langle Z^2\rangle^{1/2} \Gamma_e^{3/2} / \langle Z\rangle^{1/2}. \tag{A1}$$

Let us recall that h_{ij} is related to the reaction rates by Eq. (18). To correct our approximation in the weak-coupling limit, we note that a formal use of the linear mixing rule [employed in Eq. (23)] at low $\Gamma_{ij} \ll 1$ gives

$$h_{ij}^{lin} = 3^{-1/2} [(Z_i + Z_j)^{5/2} - Z_i^{5/2} - Z_j^{5/2}] \Gamma_e^{3/2}. \tag{A2}$$

Therefore, our fit (23) gives the correct power law ($\propto \Gamma_e^{3/2}$), but an inexact prefactor (for $0.1 \leqslant Z_1/Z_2 \leqslant 10$ and all x_1, the relative error does not exceed 40%). We suggest introducing the correction factor

$$C_{ij} = \frac{h_{ij}^{DH}}{h_{ij}^{lin}} = 3 Z_i\, Z_j \frac{\langle Z^2\rangle^{1/2}}{\langle Z\rangle^{1/2}} \frac{1}{(Z_i + Z_j)^{5/2} - Z_i^{5/2} - Z_j^{5/2}}, \tag{A3}$$

and finally write the enhancement factor as

$$h_{ij} = \frac{C_{ij} + \Gamma_{ij}^2}{1 + \Gamma_{ij}^2} \left[f_0\left(\frac{\Gamma_i}{\tau_{ij}}\right) + f_0\left(\frac{\Gamma_j}{\tau_{ij}}\right) - f_0\left(\frac{\Gamma_{ij}^{comp}}{\tau_{ij}}\right) \right], \tag{A4}$$

where τ_{ij} is given by Eq. (25). As a result, Eq. (A4) reproduces the correct Debye-Hückel asymptote of the enhancement factor in the weak coupling limit ($\Gamma_{ij} \ll 1$), and it reproduces also our results at $\Gamma \gtrsim 1$.

Our interpolation expression is certainly a simplification, but it is expected to be qualitatively correct. In Fig. 9, we show the enhancement factors h_{ij}, normalized with respect to $\Gamma_e^{3/2}$, as a function of Γ_e. We take a BIM with Z_2/Z_2 and $x_2 = 0.05$, 0.5, and 0.95 as an example. The thin dotted lines correspond to the Debye-Hückel asymptote at $\Gamma \ll 1$. The thin lines are the linear mixing asymptotes (h_{11}^{lin}, h_{12}^{lin}, and h_{22}^{lin}), which are valid in the limit of strong Coulomb coupling,

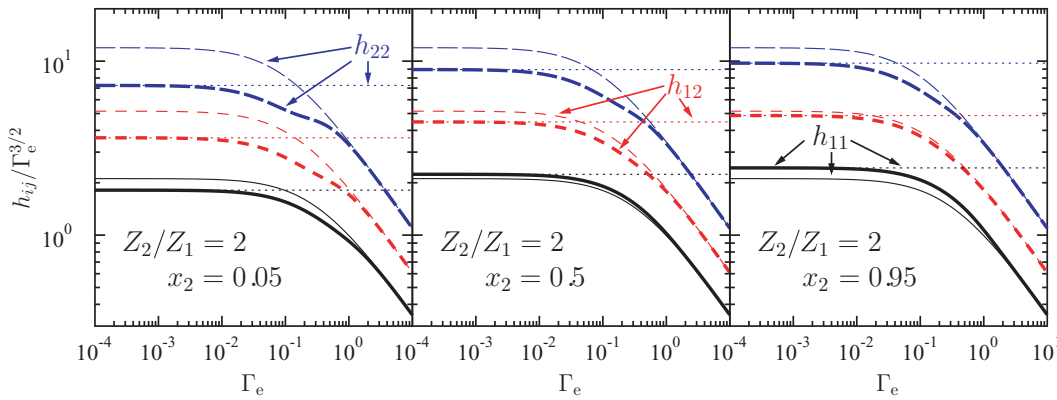

FIG. 9. (Color online) Enhancement coefficients $h_{ij}/\Gamma_e^{3/2}$ (at small ζ_{ij}) as a function of Γ_e for binary mixtures with $Z_2/Z_1 = 2$ and $x_2 = 0.05$ (left), 0.5 (center) and 0.95 (right). Thin dotted horizontal lines correspond to the Debye-Hückel enhancement (A1). Thin solid, short-dash, and long-dash lines are h_{11}^{lin}, h_{12}^{lin}, and h_{22}^{lin}, respectively. Thick lines demonstrate the enhancement factors, calculated using our interpolation expression (A4).

$\Gamma \gg 1$. The thick lines show the enhancement factors, calculated using our interpolation expression (A4). One can see that the asymptotes fix the enhancement factors quite well, and our interpolation looks reasonable.

Of course, an accurate description of the enhancement factors at moderate Coulomb coupling is desirable, but the exact solution may be complicated. Fortunately, in all cases of physical interest, the reactions in this regime occur at $\zeta_{ij} \ll 1$, so we can calculate the enhancement factors as a difference of free energies before and after a reaction event. Recent calculations of Potekhin *et al.* [35] of the free energy of binary and triple mixtures at intermediate Coulomb coupling seem to be most important in this respect. However, they are not very convenient for practical purposes, because the enhancement factors depend on derivatives of the free energy with respect to the number of particles. These derivatives should be calculated at small concentrations of compound nuclei, and the accuracy of numerical differentiation deserves a special study.

[1] D. D. Clayton, *Principles of Stellar Evolution and Nucleosynthesis* (University of Chicago Press, Chicago, 1983).
[2] P. Höflich, Nucl. Phys. **A777**, 579 (2006).
[3] T. Strohmayer and L. Bildsten, in *Compact Stellar X-Ray Sources*, edited by W. H. G. Lewin and M. Van der Klis (Cambridge University Press, Cambridge, 2006), p. 113.
[4] A. Cumming, J. Macbeth, J. J. M. in 't Zand, and D. Page, Astrophys. J. **646**, 429 (2006).
[5] S. Gupta, E. F. Brown, H. Schatz, P. Moeller, and K.-L. Kratz, Astrophys. J. **662**, 1188 (2007).
[6] D. G. Yakovlev and K. P. Levenfish, Contrib. Plasma Phys. **43**, 390 (2003).
[7] D. G. Yakovlev, K. P. Levenfish, and P. Haensel, Astron. Astrophys. **407**, 265 (2003).
[8] D. G. Yakovlev, K. P. Levenfish, A. Y. Potekhin, O. Y. Gnedin, and G. Chabrier, Astron. Astrophys. **417**, 169 (2004).
[9] D. G. Yakovlev, K. P. Levenfish, O. Y. Gnedin, Eur. Phys. J. A **25**, 669 (2005).
[10] D. Page, U. Geppert, and F. Weber, Nucl. Phys. **A777**, 497 (2006).
[11] K. P. Levenfish and P. Haensel, Astrophys. Space Sci. **308**, 457 (2007).
[12] P. S. Shternin, D. G. Yakovlev, P. Haensel, and A. Y. Potekhin, Mon. Not. R. Astron. Soc. **382**, L43 (2007).
[13] D. G. Yakovlev, L. Gasques, and M. Wiescher, Mon. Not. R. Astron. Soc. **371**, 1322 (2006).
[14] E. E. Salpeter and H. M. Van Horn, Astrophys. J. **155**, 183 (1969).
[15] L. R. Gasques, A. V. Afanasjev, E. F. Aguilera, M. Beard, L. C. Chamon, P. Ring, M. Wiescher, and D. G. Yakovlev, Phys. Rev. C **72**, 025806 (2005).
[16] D. G. Yakovlev, L. R. Gasques, M. Beard, M. Wiescher, and A. V. Afanasjev, Phys. Rev. C **74**, 035803 (2006).
[17] A. I. Chugunov, H. E. DeWitt, and D. G. Yakovlev, Phys. Rev. D **76**, 025028 (2007).
[18] J. W. Negele and D. Vautherin, Nucl. Phys. **A207**, 298 (1973).
[19] H. E. DeWitt, W. Slattery, D. Baiko, and D. Yakovlev, Contrib. Plasma Phys. **41**, 251 (2001).
[20] S. Ichimaru, Rev. Mod. Phys. **65**, 255 (1993).
[21] H. M. Van Horn and E. E. Salpeter, Phys. Rev. **157**, 751 (1967).
[22] S. Schramm and S. E. Koonin, Astrophys. J. **365**, 296 (1990); **377**, 343(E) (1991).
[23] N. Itoh, F. Kuwashima, and H. Munakata, Astrophys. J. **362**, 620 (1990).
[24] S. Ogata, Astrophys. J. **481**, 883 (1997).
[25] E. L. Pollock and B. Militzer, Phys. Rev. Lett. **92**, 021101 (2004).
[26] B. Militzer and E. L. Pollock, Phys. Rev. B **71**, 134303 (2005).
[27] A. Alastuey and B. Jancovici, Astrophys. J. **226**, 1034 (1978).
[28] B. Widom, J. Chem. Phys. **39**, 2808 (1963).
[29] B. Jancovici, J. Stat. Phys. **17**, 357 (1977).
[30] S. Ogata, H. Iyetomi, and S. Ichimaru, Astrophys. J. **372**, 259 (1991).
[31] H. DeWitt and W. Slattery, Contrib. Plasma Phys. **39**, 97 (1999).
[32] Y. Rosenfeld, Phys. Rev. E **53**, 2000 (1996).
[33] H. DeWitt, W. Slattery, and G. Chabrier, Physica B **228**, 21 (1996).
[34] H. DeWitt and W. Slattery, Contrib. Plasma Phys. **43**, 279 (2003).
[35] A. Y. Potekhin, G. Chabrier, and F. J. Rogers, Phys. Rev. E **79**, 016411 (2009).
[36] J.-M. Caillol and D. Gilles, J. Phys. A **36**, 6243 (2003).
[37] S. Ogata, S. Ichimaru, and H. M. Van Horn, Astrophys. J. **417**, 265 (1993).
[38] A. Y. Potekhin and G. Chabrier, Phys. Rev. E **62**, 8554 (2000).
[39] E. E. Salpeter, Aust. J. Phys. **7**, 373 (1954).
[40] H. E. DeWitt, H. C. Graboske, and M. S. Cooper, Astrophys. J. **181**, 439 (1973).
[41] D. G. Yakovlev and D. A. Shalybkov, Sov. Sci. Rev. E **7**, 313 (1989).
[42] L. R. Gasques, A. V. Afanasjev, M. Beard, J. Lubian, T. Neff, M. Wiescher, and D. G. Yakovlev, Phys. Rev. C **76**, 045802 (2007).
[43] N. Itoh, N. Tomizawa, S. Wanajo, and S. Nozawa, Astrophys. J. **586**, 1436 (2003).
[44] C. L. Jiang, K. E. Rehm, B. B. Back, and R. V. F. Janssens, Phys. Rev. C **75**, 015803 (2007).
[45] E. M. Kantor and M. E. Gusakov, Mon. Not. R. Astron. Soc. **381**, 1702 (2007).
[46] A. D. Kaminker, C. J. Pethick, A. Y. Potekhin, V. Thorsson, and D. G. Yakovlev, Astron. Astrophys. **343**, 1009 (1999).
[47] R. Perez-Torres, T. L. Belyaeva, and E. F. Aguilera, Phys. At. Nucl. **69**, 1372 (2006).
[48] R. L. Cooper, A. W. Steiner, and E. F. Brown, Astrophys. J. (accepted for publication), arXiv:0903.3994.